NEURAL OPERATORS WITH LOCALIZED INTEGRAL AND DIFFERENTIAL KERNELS

Anonymous authors
Paper under double-blind review

ABSTRACT

Neural operators learn mappings between function spaces, which is applicable for learning solution operators of PDEs and other scientific modeling applications. Among them, the Fourier neural operator (FNO) is a popular architecture that performs global convolutions in the Fourier space. However, such global operations are often prone to over-smoothing and may fail to capture local details. In contrast, convolutional neural networks (CNN) can capture local features but are limited to training and inference at a single resolution. In this work, we present a principled approach to operator learning that can capture local features under two frameworks by learning differential operators and integral operators with locally supported kernels. Specifically, inspired by stencil methods, we prove that under an appropriate scaling of the kernel values of CNNs, we obtain differential operators. To obtain integral local operators, we utilize suitable basis representations for the kernels based on discrete-continuous convolutions. Both these principled approaches preserve the properties of operator learning and, hence, the ability to predict at any resolution. Adding our layers to FNOs significantly improves their performance, reducing the relative L^2-error by 34-72% in our experiments on turbulent 2D Navier-Stokes fluid flow and the spherical shallow water equations.

1 INTRODUCTION

Deep learning holds the promise to greatly accelerate advances in computational science and engineering, which often require numerical solutions of partial differential equations (PDEs) (Azzizadenesheli et al., 2023; Zhang et al., 2023; Cuomo et al., 2022). Large speedups over traditional methods have been achieved by the usage of neural operators, which learn mappings between function spaces, enabling operator learning for function-valued data (Li et al., 2021; Azzizadenesheli et al., 2023; Raonić et al., 2023). In particular, they are agnostic to the discretization of the input and output functions—a vital property in the context of PDEs where data is often provided at varying resolutions and high-resolution data is costly to generate (Kovachki et al., 2021). In contrast, standard neural networks such as convolutional neural networks (CNN) (Ronneberger et al., 2015; Gupta & Brandstetter, 2022) require the functions to be discretized at a fixed resolution on a regular grid, which is limiting. In the past few years, various architectures of neural operators have been developed. Among them, the Fourier neural operator (FNO) (Li et al., 2020a) has gained popularity and shown good performance in a number of applications. However, FNO performs global convolutions in the Fourier space, which is often prone to over-smoothing and may fail to capture local details.

There are many applications that require a local neural operator, since the solution operators of many relevant PDEs are of local nature. Examples include hyperbolic PDEs, which have real-valued characteristic curves (LeVeque, 1992). As a result, a solution at a given point will only depend on the initial condition within a neighborhood of that point. As such, their solution operators only have a local receptive field and can, therefore, be efficiently learned by locally supported kernels. Another example of local operators are differential operators which can be expressed in terms of pointwise multiplication with the frequency in the spectral domain. Consequently, they introduce large errors when approximated by a finite number of parameters in Fourier space. In this context, we note that the emulation of classical numerical methods to solve partial differential equations, such as finite-difference methods, relies on the usage of local stencils for differentiation. This calls for the presence of local and differential operators in neural operator architectures.

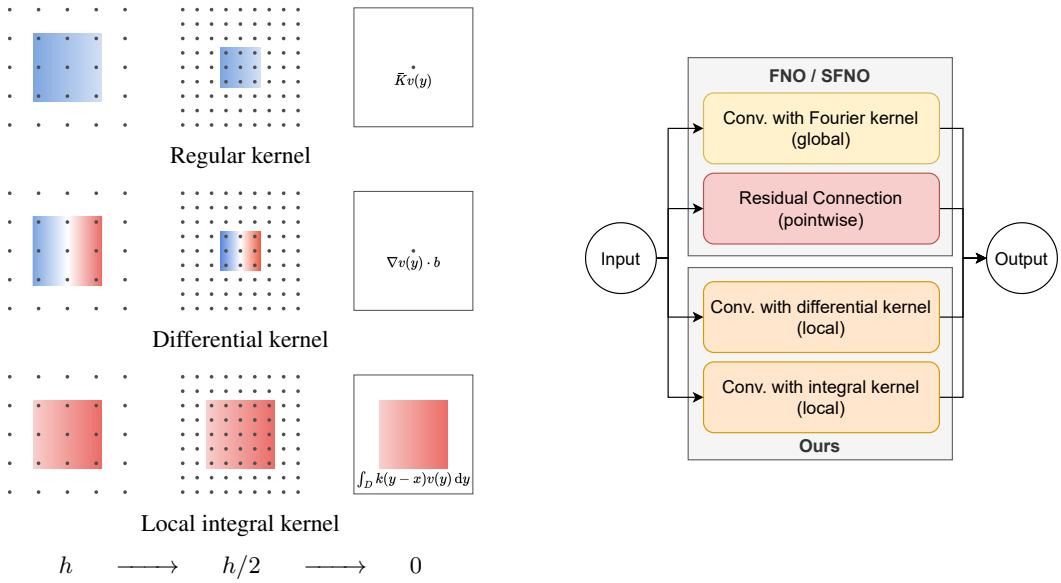

Figure 1: (**Left**): Visualization of different limits of a convolution with a discretized function v as the grid width h is refined, i.e., $h \to 0$. A regular convolution is collapsing to a pointwise linear operator (top), whereas a differential operator or a local integral operator can be achieved by correctly constraining the kernel size and weights in the limit, see Section 2. **(Right)** A single layer of our local neural operator. We add (up to) two local operations using the convolutions with differential kernel and local integral kernel (Section 2).

Naturally, every local operation can also be represented by a global operation. However, this is typically vastly parameter-inefficient and does not provide a good inductive bias for learning local operations. In the context of neural operators, spectral variants of neural operators, such as the FNO and Spherical FNO (SFNO) (Bonev et al., 2023), are theoretically able to approximate local convolutions. However, representing local kernels requires the approximation of a global signal in the spectral domain, in turn demanding a large number of parameters (due to the uncertainty principle).

A few prior works have explored the usage of local operations in the context of neural operators (see Appendix A). However, since all of the above approaches rely on standard convolutional layers on equidistant grids, they have the following shortcomings. First, such approaches do not allow for a natural extension to unstructured grids or other geometries, which are ubiquitous in PDE problems (Li et al., 2023). Moreover, they can only be applied to higher resolutions by downsampling of the (intermediate) inputs to the training resolution. Important high-frequency content can be lost through downsampling, which is particularly problematic for multi-scale data in the context of PDEs. In contrast, we develop convolutional layers that can be applied at any resolution without downsampling. We achieve this by appropriately scaling the receptive field or the values of the kernel (see Figure 1).

2 Local Layers

In this section, we develop computationally efficient and principled approaches to include operations in neural operators that capture local receptive fields, while retaining the ability to approximate operators and hence, extend to multiple resolutions. We consider two kinds of localized operators: differential operators and integral kernel operators with a locally supported kernel (see Figure 1). For the first, we draw inspiration from stencils of finite-difference methods. We derive conditions to modify convolutional layers such that they converge to a unique differential operator when the discretization is refined. For the second case of local integral operator, we adapt discrete-continuous (DISCO) convolutions (Ocampo et al., 2022) to provide an efficient, discretization-agnostic framework that can be applied to general meshes on both planar and spherical geometries.

We consider an input function $v\colon \mathbb{R}^d \supset D \to \mathbb{R}^n$ that is discretized on grids $D^h \subset D$ with width h on a domain $D = [0,1]^d$. For notational convenience, we present most ideas for the case $d = 1$, but it is straightforward to extend it to higher-dimensional domains.

Differential Layer: We construct a layer that converges to a differential operator when the width h of the discretization D^h tends to zero. To prevent the operator from collapsing to a pointwise operation (as for a standard convolution, see Appendix A.1), we constrain and rescale the values of the kernel (according to the discretization width). Note that without rescaling, we would again recover a pointwise operator; however, due to the rescaling by a factor of $\frac{1}{h}$, the limit might not exist without constraining the values of the kernel. The next proposition shows that it is sufficient to subtract the average kernel values, see Appendix B for the proof.

Proposition 2.1 (First-order differential operator)**.** *Let $D_h \subset \mathbb{R}^d$ be a regular grid of width h and let $v \in C^1(D, \mathbb{R}^n)$. Then, for every kernel $(K_s)_{s=1}^S \subset \mathbb{R}^n$, there exists $(b_i)_{i=1}^n \subset \mathbb{R}^d$ such that*

$$\lim_{h\to 0} \frac{1}{h} \operatorname{Conv}_{K-\bar{K}}[v](x) = \sum_{i=1}^{n} \nabla v_i(x) \cdot b_i$$

for every $x \in D_h$, where $\bar{K} = \sum_{s=1}^S K_s$.

Proposition 2.1 shows that we can learn different directional derivatives using an appropriate adaptation of standard convolutional layers. Specifically, we center the kernel K by subtracting its mean $\bar{K}$ and scale the result by the reciprocal resolution $\frac{1}{h}$.

Integral Kernel Layers: Instead of rescaling the kernel, we can also adapt the size of the kernel such that the receptive field stays the same, i.e., is independent of the resolution h. We will explain in the following how we can adapt the size of the kernel with a fixed number of parameters. To construct a locally supported kernel κ, we can directly discretize a convolution, i.e.,

$$\int_D k(x,y) \cdot v(x)\,\mathrm{d}x \approx \sum_{x \in D^h} \kappa(y-x) \cdot v(x)\, q_x. \tag{1}$$

Note that the sum can be taken only over the $x \in D^h$ with $y - x \in \operatorname{supp}(\kappa)$.

The remaining question is centered around the parametrization of the kernel. One could draw inspiration from works on *hypernetworks* in computer vision and parameterize it using a neural network (Shocher et al., 2020). However, this is significantly more costly than a standard convolution. Another idea is to interpolate a fixed-sized kernel, e.g., using sinc or bi-linear interpolation. A more general version of the latter, based on a learnable linear combination of hat functions, is also known as *discrete-continuous* (DISCO) convolution and has shown to be effective in different applications (Ocampo et al., 2022). We note that this formulation is closest to the original convolutional layer typically used in computer vision. However, in Appendix C we see that it also allows us to use unstructured meshes and formulate the operation on more general domains $D \subset \mathbb{R}^d$.

3 Experiments

To validate the effectiveness of local operators, we evaluate the architecture on three PDE problems. Figure 3 shows samples on two of these PDEs. In all three cases, we incorporate our proposed local layers into existing FNO and SFNO architectures to demonstrate that a significant improvement in performance can be achieved by introducing the inductive bias of local convolutions (see Figure 1 and Appendix D.1 for details on the architecture). We focus on three experimental settings: learning a differential operator in a Darcy flow problem, a 2D Navier-Stokes fluid flow with Reynolds number 5000, and the spherical shallow water equations. The detailed experimental setting, specific implementation details, and hyperparameters can be found in Appendix D.

The results of our numerical experiments are reported[1] in Table 1. We observe significant performance gains over the baselines in all three problem settings. In particular, we notice that the best performance

[1] In all three settings, hyperparameters are chosen to result in similar macro-architectures with roughly similar parameter counts for the purpose of comparability. The experimental setup including choice of hyperparameters is outlined in Section D in the Appendix.

Table 1: Experimental results for Darcy flow, Navier-Stokes, and the spherical shallow water problems. For all three problems, the test error is reported in terms of the relative L^2-loss after a single step. For the time-dependent Navier-Stokes and shallow water equations we also predict the error after 5 autoregressive steps.

PDE	Model	rel. L^2-error (1 step)	rel. L^2-error (5 steps)
Darcy Flow	U-Net	$1.380 \cdot 10^{-2}$	-
	FNO	$5.867 \cdot 10^{-2}$	-
	FNO + diff. kernel (ours)	$\mathbf{7.357 \cdot 10^{-3}}$	-
	FNO + local integral kernel (ours)	$6.034 \cdot 10^{-2}$	-
	FNO + local integral + diff. kernel (ours)	$9.032 \cdot 10^{-3}$	-
Navier-Stokes	U-Net	$1.674 \cdot 10^{-1}$	$5.115 \cdot 10^{-1}$
	FNO	$1.381 \cdot 10^{-1}$	$2.360 \cdot 10^{-1}$
	FNO + diff. kernel (ours)	$1.073 \cdot 10^{-1}$	$2.129 \cdot 10^{-1}$
	FNO + local integral kernel (ours)	$1.110 \cdot 10^{-1}$	$2.183 \cdot 10^{-1}$
	FNO + local integral + diff. kernel (ours)	$\mathbf{9.022 \cdot 10^{-2}}$	$\mathbf{1.956 \cdot 10^{-1}}$
Shallow Water	U-Net	$1.341 \cdot 10^{-3}$	$1.226 \cdot 10^{-2}$
	Spherical U-Net (with local integral kernel)	$6.160 \cdot 10^{-4}$	$3.265 \cdot 10^{-3}$
	SFNO	$9.220 \cdot 10^{-4}$	$3.185 \cdot 10^{-3}$
	SFNO + local integral kernel (ours)	$\mathbf{2.624 \cdot 10^{-4}}$	$\mathbf{5.392 \cdot 10^{-4}}$

in the reported relative L^2-errors is achieved with the inclusion of both global and local convolutions[2], despite an overall reduction in parameter count with respect to their corresponding FNO/SFNO baselines. This is particularly pronounced for the Navier-Stokes and shallow water equations, where errors can accumulate in autoregressive roll-outs. We attribute this to our models' inductive bias, allowing it to better capture the fine-grained scales and thus achieve better performance.

The Navier-Stokes problem demonstrates the efficacy of combining both differential and local integral kernels with the global convolution of the FNO. Our proposed model with these three components together outperforms models with only two of these three operations. We note that the Darcy flow problem is meant to motivate the need for our proposed differential kernels (and indeed, our best-performing model achieves 87% lower relative L^2-error than FNO). Since the ground truth operator in our Darcy problem is a differential operator, we expect (and observe) that for high accuracies, very local (i.e., differential) kernels are needed. In particular, we see that the baseline FNO performs poorly and the local integral kernels do not provide additional benefit. However, we include them in Table 1 for completeness.

4 Conclusion

In this paper, we have demonstrated a novel paradigm for local neural operators. We have shown how convolutional layers can be constrained to realize neural operators which approximate differential operators in the continuous limit. Moreover, we have derived convolutions with local integral kernels from the general notion of a kernel integral and the related graph neural operator. Finally, we have constructed localized neural operators on the sphere by leveraging discrete-continuous convolutions (Ocampo et al., 2022).

The resulting local neural operators introduce a strong inductive bias due to their formulation, which makes them symmetric (w.r.t. the underlying symmetry group) and ensures the same operation everywhere in the domain. Locality acts as a further constraint and reduces the number of parameters required to learn operators with local receptive fields. Our numerical experiments show consistent improvements when existing neural operators with global receptive fields are augmented with the proposed localized convolutions, resulting in reductions in relative L^2-error of up to 87% over the corresponding baselines. We thus expect local neural operators to play an important role in solving real-world scientific computing problems with machine learning.

[2]Similar results are also observed in the setting of zero-shot super-resolution, which are reported in Appendix D.8.

REFERENCES

Kamyar Azzizadenesheli, Nikola Kovachki, Zongyi Li, Miguel Liu-Schiaffini, Jean Kossaifi, and Anima Anandkumar. Neural operators for accelerating scientific simulations and design. *arXiv preprint arXiv:2309.15325*, 2023.

Erik J Bekkers. B-spline cnns on Lie groups. *arXiv preprint arXiv:1909.12057*, 2019.

Boris Bonev, Thorsten Kurth, Christian Hundt, Jaideep Pathak, Maximilian Baust, Karthik Kashinath, and Anima Anandkumar. Spherical fourier neural operators: Learning stable dynamics on the sphere. *arXiv preprint arXiv:2306.03838*, 2023.

Taco Cohen and Max Welling. Group equivariant convolutional networks. In *International conference on machine learning*, pp. 2990–2999. PMLR, 2016.

Salvatore Cuomo, Vincenzo Schiano Di Cola, Fabio Giampaolo, Gianluigi Rozza, Maziar Raissi, and Francesco Piccialli. Scientific machine learning through physics–informed neural networks: Where we are and what's next. *Journal of Scientific Computing*, 92(3):88, 2022.

J.R. Driscoll and D.M. Healy. Computing fourier transforms and convolutions on the 2-sphere. *Advances in Applied Mathematics*, 15:202–250, 6 1994.

Rohan Ghosh and Anupam K Gupta. Scale steerable filters for locally scale-invariant convolutional neural networks. *arXiv preprint arXiv:1906.03861*, 2019.

Jayesh K Gupta and Johannes Brandstetter. Towards multi-spatiotemporal-scale generalized pde modeling. *arXiv preprint arXiv:2209.15616*, 2022.

Erisa Hasani and Rachel A Ward. Generating synthetic data for neural operators. *arXiv preprint arXiv:2401.02398*, 2024.

Tero Karras, Miika Aittala, Samuli Laine, Erik Härkönen, Janne Hellsten, Jaakko Lehtinen, and Timo Aila. Alias-free generative adversarial networks. *Advances in Neural Information Processing Systems*, 34:852–863, 2021.

Nikola Kovachki, Zongyi Li, Burigede Liu, Kamyar Azizzadenesheli, Kaushik Bhattacharya, Andrew Stuart, and Anima Anandkumar. Neural operator: Learning maps between function spaces. *arXiv preprint arXiv:2108.08481*, 2021.

Randall J. LeVeque. *Numerical Methods for Conservation Laws*. Birkhäuser Basel, 1992.

Zongyi Li, Nikola Kovachki, Kamyar Azizzadenesheli, Burigede Liu, Kaushik Bhattacharya, Andrew Stuart, and Anima Anandkumar. Fourier neural operator for parametric partial differential equations. *arXiv preprint arXiv:2010.08895*, 2020a.

Zongyi Li, Nikola Kovachki, Kamyar Azizzadenesheli, Burigede Liu, Kaushik Bhattacharya, Andrew Stuart, and Anima Anandkumar. Neural operator: Graph kernel network for partial differential equations. *arXiv preprint arXiv:2003.03485*, 2020b.

Zongyi Li, Nikola Kovachki, Kamyar Azizzadenesheli, Burigede Liu, Andrew Stuart, Kaushik Bhattacharya, and Anima Anandkumar. Multipole graph neural operator for parametric partial differential equations. *Advances in Neural Information Processing Systems*, 33:6755–6766, 2020c.

Zongyi Li, Hongkai Zheng, Nikola Kovachki, David Jin, Haoxuan Chen, Burigede Liu, Kamyar Azizzadenesheli, and Anima Anandkumar. Physics-informed neural operator for learning partial differential equations. *arXiv preprint arXiv:2111.03794*, 2021.

Zongyi Li, Miguel Liu-Schiaffini, Nikola Kovachki, Kamyar Azizzadenesheli, Burigede Liu, Kaushik Bhattacharya, Andrew Stuart, and Anima Anandkumar. Learning chaotic dynamics in dissipative systems. *Advances in Neural Information Processing Systems*, 35:16768–16781, 2022.

Zongyi Li, Nikola Borislavov Kovachki, Chris Choy, Boyi Li, Jean Kossaifi, Shourya Prakash Otta, Mohammad Amin Nabian, Maximilian Stadler, Christian Hundt, Kamyar Azizzadenesheli, et al. Geometry-informed neural operator for large-scale 3d pdes. *arXiv preprint arXiv:2309.00583*, 2023.

Diego Marcos, Benjamin Kellenberger, Sylvain Lobry, and Devis Tuia. Scale equivariance in cnns with vector fields. *arXiv preprint arXiv:1807.11783*, 2018.

Jeremy Ocampo, Matthew A. Price, and Jason D. McEwen. Scalable and equivariant spherical cnns by discrete-continuous (disco) convolutions. *arXiv preprint arXiv:2209.13603*, 9 2022.

Md Ashiqur Rahman and Raymond A Yeh. Truly scale-equivariant deep nets with fourier layers. *arXiv preprint arXiv:2311.02922*, 2023.

Bogdan Raonić, Roberto Molinaro, Tobias Rohner, Siddhartha Mishra, and Emmanuel de Bezenac. Convolutional neural operators. *arXiv preprint arXiv:2302.01178*, 2023.

Olaf Ronneberger, Philipp Fischer, and Thomas Brox. U-net: Convolutional networks for biomedical image segmentation. In *Medical Image Computing and Computer-Assisted Intervention–MICCAI 2015: 18th International Conference, Munich, Germany, October 5-9, 2015, Proceedings, Part III 18*, pp. 234–241. Springer, 2015.

Assaf Shocher, Ben Feinstein, Niv Haim, and Michal Irani. From discrete to continuous convolution layers. *arXiv preprint arXiv:2006.11120*, 2020.

Ivan Sosnovik, Michał Szmaja, and Arnold Smeulders. Scale-equivariant steerable networks. *arXiv preprint arXiv:1910.11093*, 2019.

Ivan Sosnovik, Artem Moskalev, and Arnold Smeulders. Disco: accurate discrete scale convolutions. *arXiv preprint arXiv:2106.02733*, 2021.

Shenlong Wang, Simon Suo, Wei-Chiu Ma, Andrei Pokrovsky, and Raquel Urtasun. Deep parametric continuous convolutional neural networks. In *Proceedings of the IEEE conference on computer vision and pattern recognition*, pp. 2589–2597, 2018.

Gege Wen, Zongyi Li, Kamyar Azizzadenesheli, Anima Anandkumar, and Sally M Benson. U-fno—an enhanced fourier neural operator-based deep-learning model for multiphase flow. *Advances in Water Resources*, 163:104180, 2022.

Daniel Worrall and Max Welling. Deep scale-spaces: Equivariance over scale. *Advances in Neural Information Processing Systems*, 32, 2019.

Yichong Xu, Tianjun Xiao, Jiaxing Zhang, Kuiyuan Yang, and Zheng Zhang. Scale-invariant convolutional neural networks. *arXiv preprint arXiv:1411.6369*, 2014.

Ximeng Ye, Hongyu Li, Peng Jiang, Tiejun Wang, and Guoliang Qin. Learning transient partial differential equations with local neural operators. *arXiv preprint arXiv:2203.08145*, 2022.

Ximeng Ye, Hongyu Li, Jingjie Huang, and Guoliang Qin. On the locality of local neural operator in learning fluid dynamics. *arXiv preprint arXiv:2312.09820*, 2023.

Xuan Zhang, Limei Wang, Jacob Helwig, Youzhi Luo, Cong Fu, Yaochen Xie, Meng Liu, Yuchao Lin, Zhao Xu, Keqiang Yan, et al. Artificial intelligence for science in quantum, atomistic, and continuum systems. *arXiv preprint arXiv:2307.08423*, 2023.

A Related work and connections to other frameworks

We strive to formulate local operations that are consistent with the neural operator paradigm, which stipulates that operations within the model are independent of the discretization of input functions (Kovachki et al., 2021). In principle, this allows the evaluation of the neural operator on arbitrary meshes[3].

A few prior works have explored the usage of local operations in the context of neural operators. Li et al. (2020b) introduce graph neural operators (GNOs), which parameterize local integral kernels with a neural network. However, evaluating this network on all combinations of points to compute the integrals can make GNOs computationally expensive and slower in practice than hardware-optimized convolutional kernels. Alternatively, Ye et al. (2022; 2023) propose local neural operators by combining FNOs with convolutional layers and, similarly, Wen et al. (2022) integrate U-Nets and FNOs. Moreover, Raonić et al. (2023) propose convolutional neural operators (CNOs) by leveraging U-Nets that (approximately) respect the band-limits.

Several other discretization-independent local operations have been introduced in the deep learning literature. While some of these approaches have not detailed the connections to neural operators, they are independent of the discretization. In the following, we outline the connections between these works.

GNOs and Hypernetworks: In general, local operations can be provided by graph neural operators (GNOs) (Li et al., 2020b). The GNO is given by

$$\mathrm{GNO}_k[v](y) = \int_{U(y)} k(x,y) \cdot v(x) \,\mathrm{d}x \approx \sum_{x \in D^h \cap U(y)} k(x,y) \cdot v(x)\, q_x, \tag{2}$$

where k is a kernel (typically parametrized by a neural network) and q_x are suitable quadrature weights. While this can represent local kernel integral operators by picking a suitably small neighborhood $U(y) \subset D$, its default implementation is challenging to train, slow, and memory-intensive for general kernels $k\colon D \times D \to \mathbb{R}^n$ (Li et al., 2020c). Moreover, for an arbitrary kernel, GNO is not equivariant w.r.t. the symmetry group of the underlying domain. In particular, we lose the translation equivalence of convolutional layers for planar domains.

We remark that for our integral layer (Section 2) with an equidistant grid and constant[4] quadrature weights, $q = q_x$, evaluating $\mathrm{GNO}[v]$ at $x \in D^h$ corresponds to a standard convolution as in equation 4 with kernel $K_s = q\kappa(x - z_s)$, see Appendix C.2 for details. The advantage of the formulation in equation 1 is the fact that we can reuse the same kernel κ across different resolutions.

Fourier Neural Operator (FNO). To retain translation equivariance, we can consider kernels of the form $k(x,y) = \kappa(y - x)$ and $U(y) = y + \mathrm{supp}(\kappa)$. Then, we can rewrite the GNO as a convolution, i.e.,

$$\mathrm{GNO}_\kappa[v] = \kappa \star v. \tag{3}$$

If we are dealing with periodic functions on the torus D, we can leverage the convolution theorem to compute equation 3, i.e., $\mathcal{F}[\kappa \star v] = \mathcal{F}[\kappa] \cdot \mathcal{F}[v]$, where $\mathcal{F}$ maps functions to their Fourier series coefficients. The *Fourier Neural Operator* (FNO) now directly parametrizes $\mathcal{F}[\kappa]$ and approximates $\mathcal{F}$ using the *fast Fourier transform* given that D^h is a equidistant grid. While this leads to an efficient version of equation 2, this assumes that $\mathcal{F}[\kappa]$ has only finitely many nonzero Fourier modes—or, equivalently, that the kernel κ has full support, making equation 3 a *global* convolution.

Taking a convolutional kernel, GNOs also subsume a series of works on hypernetwork approaches for convolutional layers (Wang et al., 2018; Shocher et al., 2020).

DISCO Convolutions: We show that DISCO convolutions (Ocampo et al., 2022) represent special cases of GNOs with a convolutional kernel, which enable generalization to different geometries, and an efficient implementation, since the kernel can be pre-computed (see Section 2). In particular,

[3] As long as they are suitable for the evaluation of the numerical operations of the neural operator, such as the Discrete Fourier Transform used in the Fourier neural operator, see Section 2.

[4] This is, for instance, the case for the trapezoidal rule on a torus or for Monte-Carlo integration.

Table 2: Comparison of different architectures for the solution of PDEs. The top half enumerates architectures for planar domains and the bottom half for spherical domains. Our proposed architectures are highlighted in bold letters, and the differential and integral kernels are detailed in Section 2.

Architecture	Efficient	Receptive field	no input downsampling
GNO	✗	local/global	✓
FNO	✓	global	✓
CNO / U-Net	✓	local	✗
FNO + integral	✓	local/global	✓
FNO + differential	✓	local/global	✓
SFNO	✓	global	✓
SFNO + integral	✓	local/global	✓

DISCO convolutions are typically implemented as learnable linear combinations of fixed basis functions instead of neural networks. Moreover, they satisfy the equivariance in the limit of exact integration for special function classes.

Scale-Equivariant CNNs: In the area of computer vision, there has been a series of adaptations of CNNs to be (locally) scale-equivariant by using filter dilation, filter rescalings in the discrete domain (Rahman & Yeh, 2023; Sosnovik et al., 2021; Worrall & Welling, 2019) or the continuous domain (Xu et al., 2014; Sosnovik et al., 2019; Ghosh & Gupta, 2019), or input rescalings (Marcos et al., 2018). Moreover, filter rescaling has also been explored for more general group-convolutions (Bekkers, 2019).

Neural operators and convolutional layers: While neural operators have been developed independently of the above approaches, one can leverage similar ideas. In particular, one can rescale (up- and downsample) input and output functions of a convolutional layer or the kernel itself to obtain neural operators. We note that these approaches are in principle also applicable to a trained network (without the need for retraining).

In combination with FNOs, interpolation of the input and output functions has been explored by Wen et al. (2022). Also Ye et al. (2023; 2022) emphasized the need for local convolutions in FNOs, however, they do not discuss the application to different discretizations. Combined with a correct treatment of the bandlimit of the functions (based on Karras et al. (2021)), the convolutional neural operator Raonić et al. (2023) also uses up- and downsampling of the input and output functions to apply a U-Net architecture.

We note that for bandlimited functions sampled above the Nyquist frequency, the discrete convolutions have a unique correspondence to convolutions in function space, representing a special case of the DISCO framework. However, downsampling the input function introduces error for many cases where the input functions are not bandlimited.

To summarize, current neural operator architectures suffer from at least one of the following limitations (see Table 2): (1) they cannot succinctly represent operations with a local receptive field, e.g. FNO, or (2) they cannot be applied to different resolutions without relying on explicit up-/downsampling which may degrade performance, e.g., CNO, or (3) they cannot be scaled to obtain sufficient expressivity, since they incur prohibitively high computationally costs, such as, for instance, GNOs.

A.1 Motivation: Convolutional Layer

We take inspiration from convolutional layers, since they represent the prototypical version of an efficient, local operation in neural networks. However, we will see that they are not consistent in function spaces; in particular, they converge to a pointwise linear operator when we refine discretization of the input function v.

Let us start by recalling the definition of a convolutional layer, specifically a stride 1 convolution with n input channels, a single[5] output channel, and a kernel of (odd) size S. For this we assume a regular grid, i.e., $D^h = \{x_i\}_{i=1}^m$ with $x_{i+1} - x_i = h$, and kernel $(K_s)_{s=1}^S \subset \mathbb{R}^n$ such that

$$\mathrm{Conv}_K[v](x_i) = K \star \{v(x_i)\}_{i=1}^m = \sum_{s=1}^S K_s \cdot v(x_i - z_s), \tag{4}$$

with

$$z_s = h\left(s - 1 - \frac{S-1}{2}\right), \tag{5}$$

where we assume zero-padding, i.e., $v(x) = 0$ for $x \notin D$.

If we now take the same kernel K for finer discretizations, i.e., $h \to 0$, we see from equation 5 that $z_s \to 0$ and therefore,

$$\lim_{h\to 0} \mathrm{Conv}_K[v](x_i) = \sum_{s=1}^S K_s \cdot v(x_i), \tag{6}$$

given that the function v is continuous at x_i. In other words, the receptive field with respect to the underlying domain D is shrinking to a point and the convolutional layer is converging to a *pointwise linear operator*. One way to circumvent this issue would be to downsample the function v appropriately to a pre-defined grid. This is done for *convolutional neural operators* (CNOs) to preserve the given bandlimit, at the cost of losing high-frequency information in the input.

In section 2, we present two ways of working on different input resolutions, while not collapsing to a pointwise operator, see also Figure 1. First, we show that rescaling equation 4 by the reciprocal resolution $\frac{1}{h}$ and constraining the kernel K leads to *differential operators*. Then we define the kernel K as evaluation of a function over a fixed input domain, leading to *integral operators*.

B General differential kernels

In the following, we present the general idea for irregular grids, from which Proposition 2.1 follows as a special case. Let us first define the assumptions on our grids.

Regular discrete refinement: Let $\|\cdot\|$ be a norm on $\mathbb{R}^d$ and denote by $B_h(x) \subset \mathbb{R}^d$ the ball of radius $h \in (0, \infty)$ around $x \in \mathbb{R}^d$ w.r.t. $\|\cdot\|$. Further, let $D \subset \mathbb{R}^d$ be a domain and let $(h_\ell)_{\ell\in\mathbb{Z}}$ be a sequence that converges to zero. We call $(D_\ell)_{\ell\in\mathbb{Z}} \subset \mathbb{R}^d$ a *regular discrete refinement* with widths $(h_\ell)_{\ell\in\mathbb{Z}}$ if there exists $N \in \mathbb{N}$ such that for all $\ell \in \mathbb{Z}$ and $x \in \mathbb{R}^d$ we have that

$$|B_{h_\ell}(x) \cap D_\ell| \leq N \quad \text{and} \quad \mathrm{span}\left(\left\{\begin{bmatrix}1\\y\end{bmatrix} - \begin{bmatrix}1\\x\end{bmatrix} : y \in B_{h_\ell}(x) \cap D_\ell\right\}\right) = \mathbb{R}^{d+1}.$$

The second assumption states that we can find an *affinely independent* subset in each ball. Note that, for instance, equidistant grids satisfy these assumptions.

First-order differential operator: We want to find bounded kernels $k(x, y)\colon \mathbb{R}^d \times \mathbb{R}^d \to \mathbb{R}$ with the following property: There exist $c \in \mathbb{R}$ and $b \in \mathbb{R}^d$ such that for all $v \in C^2(D)$ with $\|\nabla^2 f\|_{L^\infty} \leq C$, all $x \in \mathbb{R}^d$, and any regular discrete refinement $(D_\ell)_{\ell\in\mathbb{Z}} \subset \mathbb{R}^d$ with widths $(h_\ell)_{\ell\in\mathbb{Z}}$ it holds that

$$\sum_{x\in B_{h_\ell}(y)\cap D_\ell} k(x, y)v(x) \to cv(y) + \nabla f(y) \cdot b, \quad \ell \to \infty. \tag{7}$$

We will now investigate which additional assumptions are needed. Let us fix $y \in \mathbb{R}^d$ and enumerate

$$(x_i)_{i=1}^n \coloneqq B_{h_\ell}(y) \cap D_\ell.$$

[5]This is for notational convenience; the extension to multiple output channels is straightforward.

Then, we can use Taylor's theorem to show that

$$\sum_{x \in B_{h_\ell}(y) \cap D_\ell} k(x,y)v(x) = \sum_{i=1}^{n} k(x_i, y) \left(f(y) + \nabla f(y) \cdot (x_i - y) + \mathcal{O}(h_\ell) \right) \tag{8}$$

$$= f(y) \sum_{i=1}^{n} k(x_i, y) + \nabla f(y) \cdot \left(\sum_{i=1}^{N} k(x_i, y)(x_i - y) \right) + \mathcal{O}(n \|k\|_{L^\infty} h_\ell). \tag{9}$$

Since the kernel and n are bounded (uniformly over $\ell \in \mathbb{N}$), we have that $\mathcal{O}(n\|k\|_{L^\infty} h_\ell) = \mathcal{O}(h_\ell)$. As we want to guarantee convergence to $cf(y) + \nabla f(y) \cdot b$ for suitable $c \in \mathbb{R}$ and $b \in \mathbb{R}^d$ (independent of y), we need to satisfy that

$$c = \sum_{i=1}^{n} k(x_i, y) \tag{10}$$

and that

$$b = \sum_{i=1}^{n} k(x_i, y)(x_i - y) \tag{11}$$

This yields the linear[6] system

$$\underbrace{\begin{bmatrix} 1 & \dots & 1 \\ x_1 - y & \dots & x_n - y \end{bmatrix}}_{\in \mathbb{R}^{(d+1) \times n}} \begin{bmatrix} k(x_1, y) \\ \vdots \\ k(x_n, y) \end{bmatrix} = \begin{bmatrix} c \\ b \end{bmatrix}. \tag{12}$$

Our assumptions on the refinement guarantee that we can find linearly independent columns such that we can solve the system. However, generally and by abuse of notation, the value of $k(x_i, y)$ also needs to also depend on the other points $(x_i)_{i=1}^n$. However, for the case of an equidistant grid, one can directly see that the convolutional kernel given in Proposition 2.1 satisfies equation 12.

Remark B.1 (Higher-order differential operator). Similar to Proposition 2.1, we could approximate k-th order differential operator with further constraints on the elements of K and a scaling factor of $\frac{1}{h^k}$. However, we do not implement them in practice, since we can also approximate higher-order derivatives by composing first-order differential layers.

C Discrete-continuous convolutions

The following section outlines the basic ideas behind discrete-continuous convolutions as introduced by (Ocampo et al., 2022). To generalize the (continuous) convolution equation 3 to Lie groups and quotient spaces of Lie Groups, we consider the group convolution (see e.g. Cohen & Welling (2016)).

C.1 General discrete-continuous convolutions

Due to the local support of the kernel in equation equation 1, allows us to efficiently evaluate local convolutions in subdomains of $\mathbb{R}^d$ using sparse matrix-vector products. However, the operation $y - x$, which shifts the convolution kernel is not well-defined on manifolds such as the sphere. To generalize the previous discussion to a Lie group G, we first replace the shift operator with the group action g and obtain the so-called group convolution.

Definition C.1 (Group Convolution)**.** Let $f, k : G \to \mathbb{R}$ be functions defined on the group G. The group convolution is given by

$$(f \star k)(g) = \int f(x)\, k(g^{-1}x)\, \mathrm{d}\mu(x) \tag{13}$$

where $g, x \in G$ and $\mathrm{d}\mu(x)$ is the invariant Haar measure on G.

[6] For fixed y.

Remark C.2. In some cases, signals are not defined on a group but rather on a quotient space G/H, where H is a subgroup of G. In such cases, a convolution may still be defined by taking $g \in G/H$. For an example see spherical convolutions (Driscoll & Healy, 1994; Ocampo et al., 2022).

This formulation presents us with the challenge of being non-trivial to discretize. While group convolutions can typically be computed by generalized Fourier transforms on the corresponding manifolds, their usage is generally preferred if the convolutions are non-local operators, i.e. the convolution kernel k is not compactly supported. On the periodic domain $\mathbb{T}^n$ (i.e. Euclidean space with periodic boundaries), convolutions are typically computed discretely by directly sliding the kernel. The framework of DISCO convolutions (Ocampo et al., 2022) achieves this by approximating the integral with a quadrature rule, while evaluating the group action continuously:

Definition C.3 (DISCO convolutions)**.** Given a quadrature rule with quadrature points $x_j \in G$ and quadrature weights q_i, we approximate the group convolution equation 13 with the discrete sum

$$(f \star k)(g) = \int f(u)\, k(g^{-1}x)\, \mathrm{d}\mu(x) \approx \sum_j k(g^{-1}x_j)\, f(x_j)\, q_j. \tag{14}$$

In particular, the group action g is applied analytically to the kernel function k, whereas the integral is approximated using the quadrature rule.

For a discrete set of output locations g_i, this becomes a straight-forward matrix-vector multiplication

$$\sum_j k(g_i^{-1}x_j)\, f(x_j)\, q_j = \sum_j K_{ij}\, f_j\, q_j \tag{15}$$

with $K_{ij} = k(g_i^{-1}x_j)$ and $f_j = f(x_j)$. In the case where k is compactly supported, K_{ij} is a sparse matrix with the number of non-zero entries per row depends on the resolution of the grid x_i and the support of k. To obtain a learnable filter, k is paramtrized as a linear combination of a chosen set of basis functions.

Although we have presented the general idea only for Lie groups G, it is possible to construct the DISCO convolution also on manifolds with a group action acting on them, such as the 2-sphere $\mathbb{S}^2$. For a detailed discussion of DISCO convolutions and a construction in one dimension, we point the reader to Ocampo et al. (2022).

Remark C.4 (Exact integration and equivariance). We note that DISCO convolutions satisfy equivariance properties for function classes which can be exactly integrated. For instance, on a an equidistant grid, these could be polynomials when using Legendre points. On the torus and equidistant grids, exact integration holds for bandlimited functions that are sampled above the Nyquist frequency.

C.2 DISCO CONVOLUTIONS IN ONE DIMENSION

For the sake of simplicity, we discuss the simple one-dimensional case on $\Omega = [0, 1]$ with periodic boundary conditions. We note that this corresponds to the circle group (or the torus) $\mathbb{T}$. For any element $y \in \Omega$, the corresponding group operation T_y is the translation $T_y : \Omega \to \Omega : x \to x \oplus y$, where we denote with $x \oplus y$ a modular shift such that the result remains in Ω.

Then, the DISCO convolution in one dimension, for Lebesgue square-integrable functions f, k becomes

$$\begin{aligned}(f \star k)(y) &= \int_{[0,1]} f(x)\, k(T_y^{-1}x)\, \mathrm{d}x = \int_{[0,1]} f(x)\, k(x - y)\, \mathrm{d}x \\ &\approx \sum_j k(x_j - y)\, f(x_j)\, q_j,\end{aligned} \tag{16}$$

for suitable quadrature points x_j with corresponding quadrature weights q_j.

Let us now consider the special case of an equidistant grid D_N with grid points $x_j = j/N$ and $y_i = i/N$ for $i, j = 0, 1, \ldots N - 1$ and a trapezoidal quadrature rule $q_j = 1/N$.

To parameterize the filter k, we pick a finite support $[0, x_{\text{cutoff}}]$ with n_k equidistant collocation points $x^{(l)}$ and corresponding hat functions. The l-th hat function is then defined as

$$k^{(l)}(x) = \begin{cases} \frac{x - x^{(l-1)}}{x^{(l-1)} - x^{(l)}} & \text{for } x^{(l-1)} \leq x < x^{(l)} \\ -\frac{x - x^{(l+1)}}{x^{(l)} - x^{(l+1)}} & \text{for } x^{(l)} \leq x < x^{(l+1)} \\ 0 & \text{else} \end{cases} . \tag{17}$$

The resulting filter is obtained as linear combination $k(x) = \sum_l^{n_k} \theta^{(l)} k^{(l)}(x)$ with trainable parameters $\theta^{(l)}$. Plugging this into equation 15, we recover the trainable DISCO convolution

$$\sum_j k(x_j - y_i)\, f(x_j)\, q_j = \sum_l^{n_k} \sum_j \theta^{(l)}\, k^{(l)}(x_j - y_i)\, f(x_j)\, q_j = \sum_l^{n_k} \sum_j \theta^{(l)} K_{ij}^{(l)}\, f_j\, q_j, \tag{18}$$

where $K_{ij}^{(l)}$ are the shifted filter functions. Let us now also assume that the collocation points coincide with the grid points, such that $x^{(l)} = x_l$. Then, due to the property of the hat functions, $K_{ij}^{(l)}$ can only contain either 0 or 1 and we obtain the circulant convolution matrices given by

$$K^{(0)} = (e_1, e_2, e_3, \ldots, e_N) \qquad K^{(1)} = (e_N, e_1, e_2, \ldots, e_{N-1}) \qquad K^{(2)} = (e_{N-1}, e_N, e_1, \ldots, e_{N-2}),$$

and so on, where e_i is the ith standard orthonormal basis vector in $\mathbb{R}^N$. This property enables an efficient implementation for regular grids on planar geometries in terms of highly-optimized CUDA kernels, based on common-place convolution layers. Moreover, this is also the case for more dimensions, where the same discrete Kernel is obtained when the kernel is continuously shifted on the grid.

C.3 DISCO CONVOLUTIONS ON THE SPHERE

For general group actions $g \in SO(3)$, the outcome of the group convolution equation 13 will be a function defined on $SO(3)$. This is due to $\mathbb{S}^2$ not being a group, but rather a manifold on which $SO(3)$ acts. We can see this by fixing the north-pole $n = [0, 0, 1]^T$ and applying any rotation $g \in SO(3)$ to it. This will trace out the whole sphere, despite the north-pole eliminating one of the Eulerian rotation angles. Therefore, to ensure that the result of the convolution is still a function defined on $\mathbb{S}^2$, we can simply restrict g in equation 13 to rotations in $SO(3)/SO(2)$, which is isomorphic to $\mathbb{S}^2$. Formally, this can be achieved by fixing the first of the three Euler angles parameterizing g to 0.

As basis functions we pick a set of piecewise linear basis functions as in equation 17. To accomodate anisotropic kernels, collocation points are distributed in an equidistant manner along both radius and circumference. More precisely, the first collocation point lies at the center, and for each consecutive ring, a fixed amount of collocation points is distributed along the circumference. The resulting basis functions are illustrated in Figure 2, for a cutoff radius of $\theta_{\text{cutoff}} = 0.1\pi$.

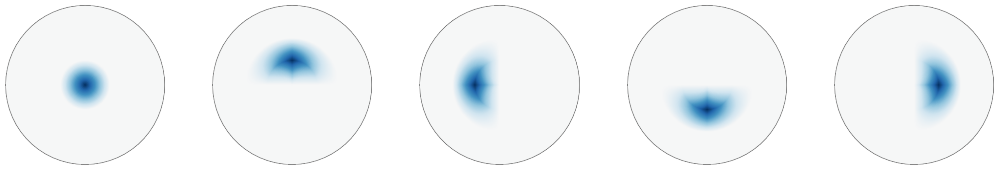

(a) $l = 0$ (b) $l = 1$ (c) $l = 2$ (d) $l = 3$ (e) $l = 4$

Figure 2: Radial, piecewise linear basis functions for the approximation of anisotropic filters on the sphere.

D EXPERIMENTAL DETAILS

Numerical comparison of our methods with baseline FNO and U-Net architectures can be found in Table 1. In this section, we outline the dataset as well as the implementation details for our numerical experiments.

In all three problems training is conducted by minimizing the squared L^2 loss until convergence is reached. A detailed experimental setup is outlined in the following subsections.

D.1 LOCAL NEURAL OPERATOR ARCHITECTURE

To design our neural operator, we want to combine pointwise, local, and global operations. To this end, we take a FNO (or SFNO for spherical problems) as a starting point, which already features global operations in Fourier space and pointwise operations using its residual connections. Then, we augment the operators by adding our proposed local convolutions from the previous section as additional branches in the respective layers (see Figure 1).

D.2 DARCY FLOW

We first consider the steady-state, two-dimensional Darcy Flow equation

$$-\nabla \cdot (a \nabla u) = f, \quad u|_{\partial D} = 0, \tag{19}$$

on the domain $D = (0, 1)^2$. In this problem, we motivate the need for incorporating local operators as inductive biases in neural operator architectures. To this end, we explicitly construct a problem which requires approximating the forcing function f for given diffusion coefficient a and pressure u. In other words, the tasks consists of learning the differential operator

$$u \mapsto -\nabla \cdot (a \nabla u). \tag{20}$$

Following the setup of Hasani & Ward (2024), we take

$$a(x) = \begin{bmatrix} x_1^2 & \sin(x_1 x_2) \\ x_1 + x_2 & x_2 \end{bmatrix} \tag{21}$$

and

$$u(x) = \sum_{i,j=1}^{20} \frac{c_{ij}}{\sqrt{\lambda_{ij}}} \sin(i\pi x_1) \sin(j\pi x_2), \tag{22}$$

for $x \in D$, where,

$$\begin{aligned} \lambda_{ij} &= (i\pi)^2 + (j\pi)^2 \\ c_{ij} &\sim \mathcal{N}(0, 1/(i+j)) \end{aligned}$$

We then compare the performance of our proposed models: FNO in parallel with differential kernels, FNO with integral kernels, and FNO with both kernels. We also compare with a baseline FNO and the U-Net architecture from Gupta & Brandstetter (2022). Moreover, we perform zero-shot super-resolution on this problem; these results can be found in Appendix D.8.

D.3 NAVIER-STOKES EQUATION

Next, we consider the two-dimensional Navier-Stokes equation on the torus. In particular, we consider Kolmogorov flows, which can be described by

$$\begin{aligned} \partial_t u + u \cdot \nabla u - \frac{1}{\text{Re}} \Delta u &= -\nabla p + \sin(ny)\hat{x} \\ \nabla \cdot u &= 0 \end{aligned} \tag{23}$$

on the spatial domain $D = [0, 2\pi]^2$ equipped with periodic boundary conditions. In the above, u and p denote the velocity and pressure, and Re denotes the Reynolds number of the flow. We want to learn the solution operator mapping initial conditions $u(\cdot, 0) = u_0$ to the time-evolved solution in vorticity form $w(\cdot, \tau)$ at time $\tau \in (0, \infty)$, where the vorticity is given by

$$w = (\nabla \times u)\hat{z}, \tag{24}$$

where $\hat{z}$ an unit vector normal to the plane.

We use the dataset from Li et al. (2022), which sets $n = 4$ and $\text{Re} = 5000$ in equation 23 and uses a temporal discretization of $\tau = 1$ on a 128×128 regular grid. The initial conditions are sampled from

a Gaussian measure as described in Li et al. (2022), and the equation is solved with a pseudo-spectral solver. We emphasize that learning the solution operator for such a high Reynolds number is very challenging due to the turbulent nature and small-scale features of the flow. We conjecture that the baseline FNO is prone to oversmoothing over the finer scales, consequently leading to a degradation of performance.

To validate this conjecture, we compare the performance of the local neural operator with a baseline FNO and U-Net and evaluate the effectiveness of our proposed differential and integral kernels, respectively.

D.4 SHALLOW WATER EQUATIONS

Finally, we test our proposed architecture on the shallow water equations on the rotating sphere. They represent a system of hyperbolic partial differential equations used to model a variety of geophysical flow phenomena, such as atmospheric flows, tsunamis, and storm surges. They can be formulated in terms of the evolution of two state variables φ and u (geopotential height and the tangential velocity of the fluid column), governed by the equations

$$\begin{aligned} \partial_t \varphi + \nabla \cdot (\varphi u) &= 0, \\ \partial_t (\varphi u) + \nabla \cdot F &= S, \end{aligned} \tag{25}$$

on the sphere $D = \mathbb{S}^2$ with suitable initial conditions $\varphi(\cdot, 0) = \varphi_0$ and $u(\cdot, 0) = u_0$, a momentum flux tensor

$$F_{ij} = \varphi u_i u_j + \frac{1}{2}\varphi^2, \tag{26}$$

and a source term

$$S(x) = -2\Omega x \times (\varphi u), \quad x \in \mathbb{S}^2, \tag{27}$$

which models the Coriolis force due to the rotation of the sphere with angular velocity Ω. We use the dataset from Bonev et al. (2023), which uses a Gaussian random field to generate initial conditions on the sphere at a resolution of 256×512 and solves for φ, u at a lead time of one hour. The target solution is computed using a spectral solver, which takes 24 Euler steps to compute the reference[7].

As baselines we use a planar U-Net architecture, a spherical U-Net, where convolutions are replaced with convolutions with local integral kernels on the sphere, and a SFNO architecture. On the sphere, we only consider the impact of the integral kernel on the SFNO architecture, as it allows for a natural extension to the sphere, see Appendix C.1.

D.5 2D DARCY FLOW EQUATION

In the 2D Darcy flow setting, we generate our data as described in Appendix D.2. We train and test our models and baselines with data discretized onto a 256×256 regular grid. As a baseline, we compare our proposed models with FNO (Li et al., 2020a) and the U-Net architecture in Gupta & Brandstetter (2022). We note that this U-Net architecture does not enjoy the property of discretization convergence (Kovachki et al., 2021). We compare these baselines against our proposed models: the architecture using convolutions with Fourier (i.e., FNO) differential, and integral kernels (Figure 1), as well as architectures using only FNO and differential kernels and only FNO with the proposed integral kernels. The results are shown in Table 1.

We choose all hyperparameters such that the overall number of parameters of all compared models is similar. The number of layers, number of Fourier modes, and embedding dimension are shown in Table 3. Models using convolutions with differential and local integral kernels use these layers in parallel to the Fourier layers and pointwise skip connection on all layers. For all relevant models, the local integral kernels use a radius cutoff of 0.007 on the unit square, and they are parameterized by five radial, piecewise linear basis functions for the approximation of anisotropic filters (analogous to Figure 2 on the plane). The differential kernels are parameterized as 3×3 2D convolutional kernels over the regular grid.

Our U-Net baseline is adapted from the model and code from the PDE Arena benchmark (Gupta & Brandstetter, 2022). In particular, we use 3×3 convolutional kernels with 2 residual blocks for

[7]The dataset and solver are taken from the `torch-harmonics` package at `https://github.com/NVIDIA/torch-harmonics`.

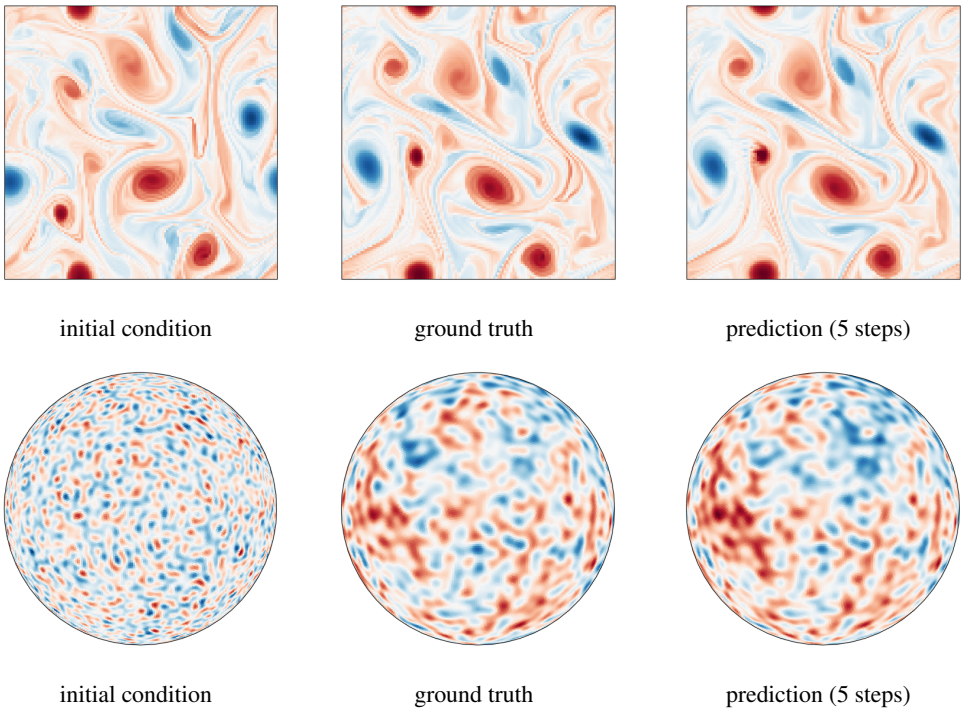

Figure 3: Initial condition, ground truth, and corresponding autoregressive predictions of our proposed models for the Navier-Stokes problem (top row) and the shallow water equations (bottom row).

each resolution (two downsampling and two upsampling), and three layers within each block, with channel multipliers of $1, 2, 4$ for each layer within a block.

For the Darcy problem, we find empirically that our models with local differential kernels are more parameter efficient and achieve better performance than the baseline FNO when the number of Fourier modes is low and the embedding dimension is high. We conjecture that this increased embedding dimension confers additional expressivity to the differential kernels for learning the ground-truth differential operator. This also suggests that differential operators are an important inductive bias for this problem, as expected. We find that a baseline FNO model (no local integration or differential convolutions) with fewer modes and greater embedding dimension performed much worse than the baseline FNO model described above. We found an analogous result for the FNO + integral kernel model with fewer modes and a larger embedding dimension.

We use GELU activations for all experiments. We use reflective padding for the convolutional operations in the differential and local integral kernels. Training is conducted by minimizing the squared L^2 loss for 70 epochs on a single NVIDIA RTX P100 GPU, which is sufficient to achieve convergence on all models. We used a step learning rate decay scheduler, starting at 10^{-3} and halving every 10 epochs.

D.6 2D Navier-Stokes Equations

For the 2D Navier-Stokes equations, we use the same experimental setup and dataset as Li et al. (2022). The data is discretized onto a 128×128 regular grid. The particular form of the Navier-Stokes equation that we consider is a 2D Kolmogorov flow with a Reynolds number of 5000. We compare the same five models as in the Darcy experiment.

As in the Darcy setting, we choose all hyperparameters such that overall number of parameters for all the models is similar. The number of layers, number of Fourier modes, and embedding dimension are shown in Table 3. Models using convolutions with differential and local integral kernels use these layers in parallel to the Fourier layers and pointwise skip connection on all layers. For all relevant

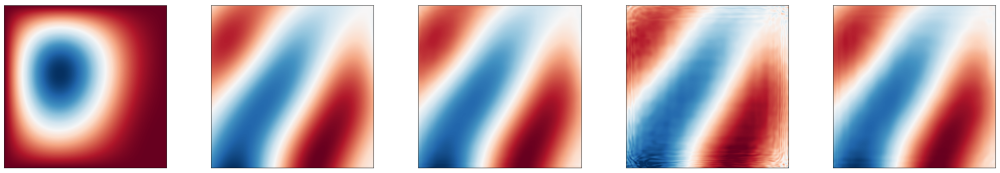

(a) Input (b) Ground truth (c) Ours (d) FNO (e) U-Net

Figure 4: Comparison of models from Table 1: The outputs of our best-performing model, FNO, and U-Net on a randomly-selected input pressure function from the Darcy flow problem. Edge artifacts are very prevalent on the FNO predictions, and they are less dominant in the U-Net predictions.

models, the local integral kernels use a radius cutoff of 0.05π on the torus, and they are parameterized by five radial, piecewise linear basis functions for the approximation of anisotropic filters (analogous to Figure 2 on the plane). The differential kernels are parameterized as 3×3 2D convolutional kernels over the regular grid.

For the Navier-Stokes setting, we find empirically that our models with local integral kernels are more parameter efficient and achieve better performance than the baseline FNO when the number of Fourier modes is low and the embedding dimension is high. We conjecture that this allows the Fourier features to learn the global, low-frequency components of the solution, while the high-frequency components are captured by the local operators. This also suggests that local convolutions are an important inductive bias for this problem. We find that a baseline FNO model (no local integration or differential convolutions) with fewer modes and greater embedding dimension performed much worse than the baseline FNO model described above. We found an analogous result for the FNO + diff. kernel model with fewer modes and a larger embedding dimension.

Out U-Net baseline is set up in the same way as in the Darcy experiment. The specific number of layers and embedding dimension is given in Table 3. We use GELU activations for all experiments. We enforce periodic boundary conditions during padding for the convolutional operations in the differential and local integral kernels. Training was performed for 136 epochs on a single NVIDIA RTX 4090 GPU. We used a step learning rate decay scheduler, starting at 10^{-3} and halving every 33 epochs.

D.7 Shallow water Equations

For the shallow water equations, we use the dataset presented in (Bonev et al., 2023). To generate samples, initial conditions are drawn from a Gaussian Random Process at resolution of 256×512 on an equiangular lat-lon-grid and then advanced in time using a numerical spectral solver. Physical constants such as the sphere's radius or the Coriolis force are set to match those of Earth. The numerical solver uses 150 explicit Euler steps to advance the solution 1 hour in time. The right-hand side is discretized using the spectral basis provided by the Spherical Harmonics. For a detailed description of the dataset, we refer the reader to (Bonev et al., 2023) and the corresponding implementation in the `torch-harmonics` package.

As a baseline for our experiments, we use the SFNO architecture as presented in Bonev et al. (2023), where the embedding dimension is adjusted to 32 to obtain a manageable parameter count. Moreover, we adapt the U-Net architecture in Gupta & Brandstetter (2022) to the spherical domain by replacing all spatial (not 1×1) convolutions to DISCO convolutions on the sphere. The resulting architecture is therefore a spherical U-Net similar to the U-Net architecture presented in Ocampo et al. (2022). Moreover, due to the DISCO convolutions's discretization-invariant nature, this architecture can be interpreted as a neural operator. Finally, we augment the SFNO architecture with local (DISCO) convolutions to obtain the proposed architecture. For all experiments GELU activation functions are used.

For all three architectures, hyperparameters were chosen to achieve roughly similar parameter counts. The learning rates for each architecture were determined with a quick parameter sweep and we use $3 \cdot 10^{-4}$ for the spherical U-Net and $3 \cdot 10^{-3}$ for both neural operators. Training was performed for 100 epochs on a single NVIDIA RTX A6000 GPU, which was sufficient to achieve convergence on

Table 3: Overview over the hyperparameters selected for out different experiments and architecture.

Model	Parameters			
	# Layers	# Modes	Embedding	# Parameters
Darcy Flow				
U-Net	17	-	18	$2.850 \cdot 10^6$
FNO	4	20	41	$2.715 \cdot 10^6$
FNO + diff. kernel (ours)	4	12	65	$2.638 \cdot 10^6$
FNO + local integral kernel (ours)	4	20	40	$2.617 \cdot 10^6$
FNO + local integral + diff. kernel (ours)	4	12	64	$2.639 \cdot 10^6$
Navier-Stokes Equations				
U-Net	17	-	56	$2.758 \cdot 10^7$
FNO	4	40	65	$2.711 \cdot 10^7$
FNO + diff. kernel (ours)	4	40	65	$2.726 \cdot 10^7$
FNO + local integral kernel (ours)	4	20	129	$2.716 \cdot 10^7$
FNO + local integral + diff. kernel (ours)	4	20	127	$2.691 \cdot 10^7$
Spherical Shallow Water Equations				
U-Net	17	-	32	$2.898 \cdot 10^6$
Spherical U-Net (with local integral kernel)	17	-	32	$1.639 \cdot 10^6$
SFNO	4	128	32	$1.066 \cdot 10^6$
SFNO + local integral kernel (ours)	4	128	31	$1.019 \cdot 10^6$

Table 4: Zero-shot super-resolution results for Darcy flow and the spherical shallow water problems. The validation error is reported in terms of relative L^2 loss at double the training resolution. Autoregressive rollouts are super-resolved in the sense that the rollout is performed at the high resolution.

Model	Relative L^2 Error. (super-res.)	
	1 step	5 steps
Darcy Flow		
FNO	$8.646 \cdot 10^{-2}$	-
FNO + diff. conv. (ours)	$\mathbf{7.774 \cdot 10^{-2}}$	-
Spherical Shallow Water Equations		
Spherical U-Net (with local integral conv.)	$3.386 \cdot 10^{-3}$	$1.244 \cdot 10^{-2}$
SFNO	$3.830 \cdot 10^{-3}$	$1.427 \cdot 10^{-2}$
SFNO + local integral conv. (ours)	$\mathbf{3.232 \cdot 10^{-3}}$	$\mathbf{7.450 \cdot 10^{-3}}$

all considered models. As learning rate scheduler, we use the popular policy of halving the learning rate upon a plateauing of the loss.

D.8 Zero-shot super-resolution results

In this paper we propose two methods to embed the inductive biases of learning local operators into neural operator architectures. The key distinction between our proposed methods and CNN-based architectures is that our methods are agnostic to the discretization of the input function. In this section, we present and discuss the super-resolution capabilities of our proposed models. In particular, we focus on two examples: (1) the Darcy flow equation to showcase our differential layers on a regular Cartesian grid and (2) the shallow water equation to demonstrate super-resolution for our local integration on the sphere. The experimental setting that we consider is that of *zero-shot super-resolution*. In particular, suppose that the model has been trained at a particular training resolution

(or at multiple different resolutions). The task of zero-shot super-resolution is to then input a function that is of higher resolution than the training resolution and evaluate the resulting model error.

In the Darcy flow setting, we use the same setup and dataset as described in Appendix D.2. We train two models on data sampled at a 256×256 regular grid and evaluate on a 512×512 regular grid (2x super-resolution and 4x the number of points). For the shallow water equations, a similar approach is taken. We take the models in Appendix D.4 which were trained at a resolution of 256×512 and apply them to data generated at a resolution of 512×1024.

Table 4 lists the results of our super-resolution experiment with our proposed models. In the Darcy setting, we compare the baseline FNO to the FNO augmented with differential convolution. On the sphere, we make use of the fact that the spherical U-Net presented in Ocampo et al. (2022) is already a neural operator, due to its discretization-independence. As such, we can use it alongside the SFNO as a baseline for zero-shot super-resolution on the sphere.

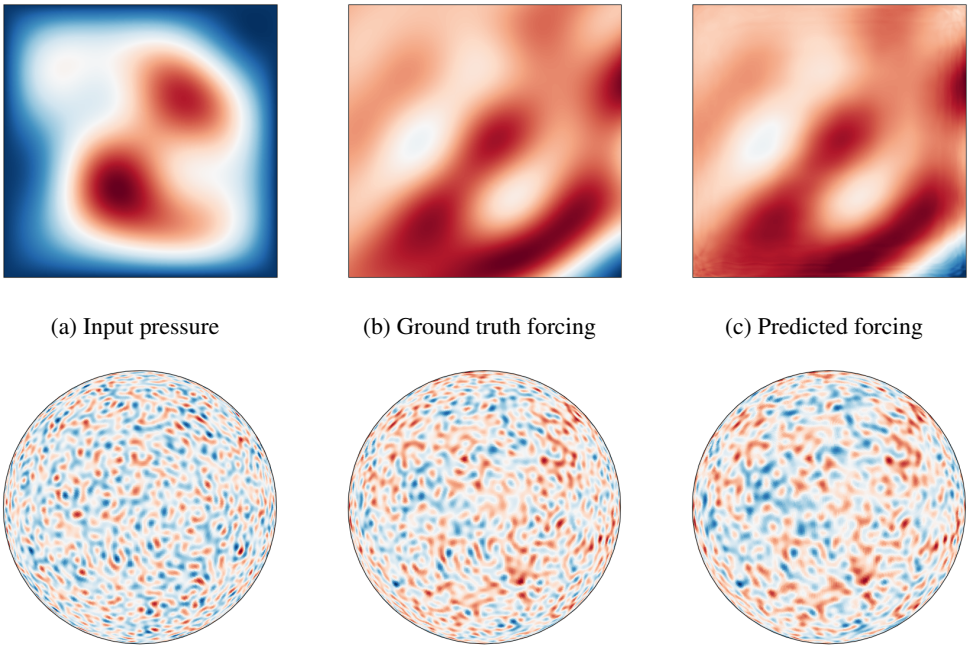

(a) Input pressure (b) Ground truth forcing (c) Predicted forcing

(d) Initial geopotential height (e) Ground truth at 1h (f) Prediction at 1h

Figure 5: Randomly-selected super-resolution samples for the Darcy flow (top row) and shallow water (bottom row) problems.

As with all neural operator architectures, during training there is the possibility of overfitting to the training resolution. For instance, FNO may learn features in Fourier space that are intrinsically tied to the resolution of the input function. Similarly, it is possible that our proposed differential and integral convolutional operators will learn a function of the training discretization. This effect can be remedied by using high-resolution training data where the local details are fully-resolved. This minimum required resolution of the training data is thus a function of the smoothness of the input function. For this reason, we decided to exclude the 2D Navier-Stokes problem from our super-resolution experiments, since training at a resolution that sufficiently-resolves the local dynamics would be prohibitvely expensive.

In our experiments, we noticed that our differential layers tend to incur some discretization error when trained on data that is not of sufficiently-high resolution, and if differential convolutions are present in consecutive layers in the model, this error can propagate quickly. As such, we found that the best-performing model on zero-shot super-resolution for the Darcy flow problem is a model with a differential convolution in only the first layer. As with the Navier-Stokes setting, we note that training at a sufficiently-high resolution so that the discretization error incurred by the differential

convolutions is negligible would be prohibitively expensive. Using fewer differential layers in our model reduces the expressivity, but we find that the super-resolution capabilities are still better than the baseline FNO.

Lastly, we would like to note that in our experiments FNO had larger error near the boundary in non-periodic problems, as the FFT used in FNO assumes periodic boundary conditions. We note that our proposed differential can help reduce the error at the boundary that is caused by FNO, but some of these effects may still be present (see Figure 5).